RESEARCH ARTICLE | APRIL 01 2026

Robust Mottness and tunable interlayer magnetism in Nb_3X_8 (X = F, Cl, Br, I) bilayers

Zhongqin Zhang ; Jiaqi Dai; Cong Wang ; Zhihai Cheng ; Wei Ji

APL Computational Physics 2, 026102 (2026)
https://doi.org/10.1063/5.0320484

APL Computational Physics ARTICLE pubs.aip.org/aip/aco

Robust Mottness and tunable interlayer magnetism in Nb_3X_8 (X = F, Cl, Br, I) bilayers

Cite as: APL Comput. Phys. 2, 026102 (2026); doi: 10.1063/5.0320484
Submitted: 31 December 2025 • Accepted: 17 March 2026 •
Published Online: 1 April 2026

Zhongqin Zhang,[1,2] Jiaqi Dai,[1,2] Cong Wang,[1,2,a)] Zhihai Cheng,[1,2] and Wei Ji[1,2,a)]

AFFILIATIONS

[1] Beijing Key Laboratory of Optoelectronic Functional Materials and Micro-Nano Devices, School of Physics, Renmin University of China, Beijing 100872, China
[2] Key Laboratory of Quantum State Construction and Manipulation (Ministry of Education), Renmin University of China, Beijing 100872, China

[a)] **Authors to whom correspondence should be addressed:** wcphys@ruc.edu.cn and wji@ruc.edu.cn

ABSTRACT

Breathing kagome materials Nb_3X_8 (X = F, Cl, Br, I) have attracted broad interest owing to their Mott insulating behavior and stacking-dependent magnetic ground states. However, the role of interlayer coupling in modulating these properties remains underexplored. Here, using density functional theory with Hubbard *U* corrections, we systematically investigated how interlayer coupling affects the Mott insulating states and magnetic ground states across 24 bilayer stacking configurations for each compound. We found that all bilayers remain Mott insulators, demonstrating robust Mottness. Driven by the competition between interlayer Pauli repulsion and hopping, most stackings favor interlayer AFM order, including conventional and compensated AFM, while some exhibit AFM-FM degeneracy or stabilize interlayer FM. This robustness of Mott states coexisting with tunable interlayer magnetism provides novel analysis and insights for research on breathing kagome Mott insulators.

I. INTRODUCTION

Kagome-lattice materials are exceptional material platforms for exploring the interplay among electronic band topology, strong electron correlation, and magnetism in quantum materials.[1–7] The standard kagome tight-binding model is two-dimensional (2D) and exhibits a flat band across the entire Brillouin zone, Dirac cones at the K points, and van Hove singularities located at the M points. Theoretical studies predict that tuning electron filling within these kagome bands can stabilize diverse exotic phases, such as magnetism,[8,9] superconductivity,[10,11] and charge-density wave states.[12] Experimental investigations, however, have primarily focused on three-dimensional (3D) bulk kagome materials, such as CsV_3Sb_5[7,13,14] and Co_3SnS_2.[15–17] In these systems, interesting phenomena, such as superconductivity,[13,14] pair-density wave,[7] charge order,[13] and spin–orbit polarons,[15] have been reported. In bulk crystals, intrinsic kagome layers typically alternate with spacer layers. The strong interlayer hybridization between them[18] often shifts or even eliminates the characteristic kagome bands near the Fermi level,[18,19] thereby obscuring the exploration of intrinsic kagome physics.

Significant effort has recently been devoted to constructing 2D kagome lattices with minimal interlayer coupling.[4] Strategies include surface-assembled organic kagome monolayers,[20–22] $MoTe_{2-x}$ monolayers with mirror-twin-boundary loops,[9,23,24] atomic intercalation within van der Waals (vdW) layers,[25,26] and a recently highlighted 3 + 1 protocol.[27] Among them, Nb_3X_8 (X = Cl, Br, I) is a prototypical layered breathing kagome family, with adjacent layers weakly coupled through vdW interactions.[28–35] Monolayer Nb_3Cl_8 and Nb_3Br_8 are established Mott insulators, characterized by well-defined upper and lower Mott–Hubbard bands around the Fermi level.[30,36] Their bulk counterparts, however, exhibit more complicated behaviors, particularly in magnetism.[33,34] Bulk Nb_3Cl_8 and Nb_3Br_8 undergo structural transitions at ~100 and 380 K, respectively. These structural changes are accompanied

by a magnetic transition from Curie–Weiss paramagnetism (PM) in the high-temperature (HT) phase to a likely nonmagnetic (NM) state at lower temperatures (LT).[33,34] Interestingly, these contrasting magnetic states differ structurally in their stacking sequences only. Moreover, the two previously proposed mechanisms for the LT NM state are both closely related to interlayer couplings,[33,34] further highlighting the importance of interlayer interactions in Nb_3X_8.

Interlayer coupling, a unique feature of 2D materials, has been increasingly recognized as an effective route to tune electronic band gaps,[37,38] optical[39,40] and acoustic properties,[41] magnetism,[42–45] and electric polarization.[46,47] Recently, it was found that interlayer coupling in bilayer 1T-$NbSe_2$ can transform it from a correlated insulator into a nonmagnetic band insulator, raising a crucial question: what is the role of interlayer coupling in electronic structures of kagome-based Nb_3X_8 bilayers? In this article, we theoretically investigated the roles of interlayer coupling in tuning the electronic structures and magnetism in Nb_3X_8 (X = F, Cl, Br, I) bilayers using density functional theory (DFT) with Hubbard corrections. We first identified out-of-plane (OOP) electric polarization and a robust Mott–Hubbard gap in Nb_3X_8 monolayers using spin polarized bandstructure calculations with varying U. While dynamical mean field theory (DMFT) is the benchmark for Mott systems, past works have shown that DFT+U offers a computationally efficient and reliable means to capture the essential physics of Mott insulating phases.[48–51] Next, we compared the total energies of 24 stacking configurations for each compound among NM and interlayer AFM and FM states. Most bilayers favor interlayer AFM, while a few exhibit AFM-FM degeneracy or interlayer FM. All bilayers remain Mott insulators, as verified by real-space wavefunction distributions, bandstructures, and U dependence. Symmetry analyses uncover compensated AFM states, classifying all studied configurations into three types of stacking-dependent and tunable interlayer magnetism. This robustness of Mott states coexisting with tunable interlayer magnetism contrasts sharply with the behaviors of transition-metal dichalcogenide-based Mott insulators.

II. RESULTS AND DISCUSSION

A. Structures and electronic bands of Nb_3X_8 monolayers

A free-standing Nb_3X_8 monolayer adopts a breathing kagome geometry [Figs. 1(a) and 1(b)], in which compact Nb_3 trimers (shaded in orange) corner-share with expanded Nb triangles (shaded in gray), giving rise to alternating short (d_{Nb1}) and long (d_{Nb2}) Nb–Nb bonds. The halogen atoms bonded to these triangular units form two inequivalent sublayers. In the lower sublayer, three equal-height halogen atoms lie beneath the expanded Nb triangle, giving a shorter vertical distance to the Nb plane (d_{XS}) than that of the halogens in the upper sublayer (d_{XL}), as shown in Fig. 1(c). The remaining halogen atom in the lower sublayer, residing beneath the compact trimer [X-s, purple, Figs. 1(a)–1(c)], is displaced further away from the Nb plane by Δ_S relative to the other three halogens in the same sublayer. In the upper sublayer, the halogen sitting above the expanded triangle (X-l, pink) is shifted closer to the Nb plane by Δ_L compared with the other three upper-sublayer halogens. We denote the lower and upper sublayers as X-s and X-l, respectively.

For Nb_3F_8, the Nb–Nb bond length in the Nb_3 trimer (d_{Nb1}) contracts to 2.59 Å, well below the Nb–Nb bonds in bulk Nb (~2.86 Å), whereas in the other Nb halides, d_{Nb1} is comparable to or larger than the bulk value. This pronounced contraction of d_{Nb1} indicates strong trimer compression and thereby enhances the X-s displacement (Δ_S). Table I compiles the two ratios Δ_S/d_{XS} and Δ_L/d_{XL} for all four Nb halides. With the sole exception of Δ_S/d_{XS} in Nb_3F_8 (0.44), which is anomalously large, the other seven entries decrease monotonically as X is varied from I to F. These opposite out-of-plane (OOP) displacements (Δ_S and Δ_L) and inequivalent distances (d_{XS} and d_{XL}) lead to a net OOP electric polarization for each Nb halide, with Nb_3F_8 exhibiting the largest value of 1.26 pC/m [Table I, Fig. 1(c)].

We compared the total energies of seven magnetic configurations for each Nb_3X_8 monolayer to find the most favored magnetic configuration among them, as shown in Fig. S1 of the supplementary material . The triangularly arranged Nb atoms in a Nb_3 trimer have geometric frustration, which, however, favor a FM nearest neighboring coupling, thereby exhibiting a shared local magnetic moment on the trimer. Therefore, we treated the Nb_3 trimer as a single entity with the +8 oxidation state. The valence electron configuration of the trimer, as shown in Fig. 1(d), includes one unpaired electron and six paired electrons, exhibiting a magnetic moment of 1 μ_B. Thus, the triangularly arranged trimers form a triangular lattice of $S = 1/2$ sites. While either the Nb_3Br_8 or Nb_3I_8 monolayer favors an FM configuration, Nb_3Cl_8 has nearly degenerate FM, ZZ-AFM and stripe-AFM configurations (Table S1), consistent with the literature.[30,52,53] However, the ZZ-AFM configuration is slightly stabilized in Nb_3F_8 (0.25 meV/Nb_3 more stable than the stripe-AFM configuration). Based on energy comparisons among the various magnetic configurations, we derived the nearest-neighbor (J_1) and next-nearest-neighbor (J_2) spin-exchange coupling constants among these Nb_3 trimers [indicated by red and blue arrows, respectively, in Fig. 1(b)], which are summarized in Table I. While J_2 consistently favors FM in all four monolayers, J_1 undergoes a gradual transition from strong FM in Nb_3I_8 and Nb_3Br_8 to weak FM in Nb_3Cl_8, and eventually to strong AFM in Nb_3F_8. This transition is closely related to the substantially reduced inter-trimer distance (d_{Nb2}, Table I). Each Nb_3X_8 monolayer exhibits easy-plane anisotropy in the xy plane, with the magnetic anisotropy energy ranging from 0.11 to 0.38 meV/Nb_3 (Fig. S3, Table S2). For such low-dimensional $S = 1/2$ systems, easy-plane magnetic anisotropy tends to amplify quantum spin fluctuations. Among the four monolayers, the smallest anisotropy energy and the competing interactions between J_1 and J_2 make Nb_3Cl_8 a promising candidate for spin liquid.[30]

Monolayer Nb_3Cl_8[30–32] or Nb_3Br_8[28,29] has been identified as a Mott insulator in previous DMFT[30,31] and model-based[28,29,32] calculations. A spin non-polarized DFT calculation reveals, for instance, Nb_3Cl_8 with a partial (half)-occupied spin-degenerate quasi-flat band that cuts the Fermi level, as plotted in Fig. 1(e). This degeneracy lifts in a spin-polarized bandstructure with the FM configuration, splitting the partial occupied band into a fully occupied and an empty spin-polarized band [Figs. 1(f) and S4(e)], as a result of the electron exchange effect. To capture the additional role of electron correlations in the exchange splitting, we incorporate an on-site Hubbard U energy to correct the self-interaction error of DFT and localize electronic wavefunctions. Consequently, both the energy gap at the Γ point [Fig. 1(g)] and the global band gaps [Fig. S4(f)] increase linearly with U, exhibiting a signature characteristic of Mott insulators. This physical picture of Mottness is consistent with that

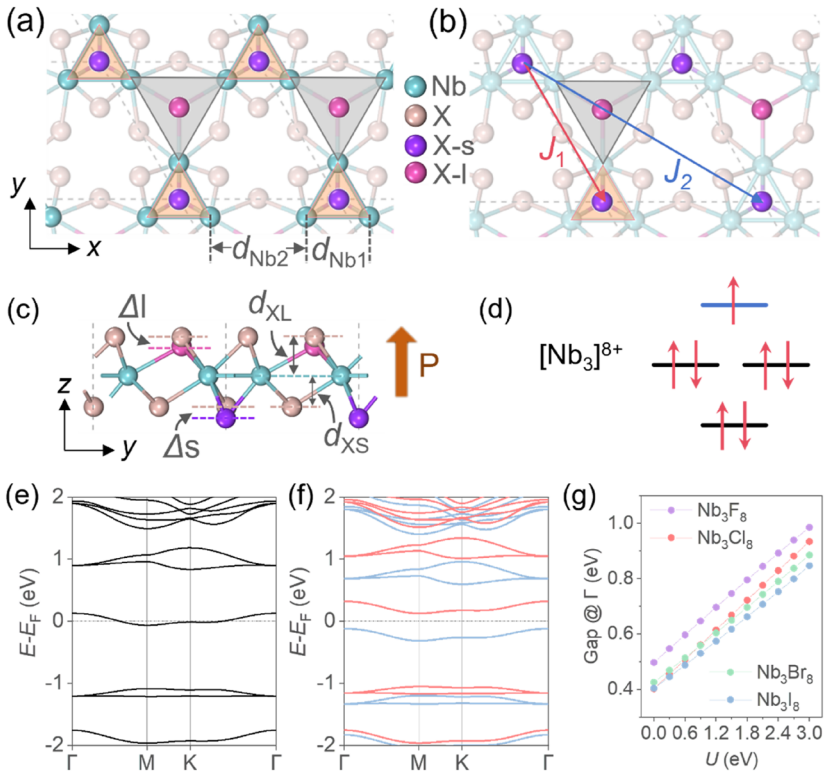

FIG. 1. (a)–(c) Top (a) and (b) and side (c) views of a monolayer Nb_3X_8. The Nb atoms are represented by light sea green balls. The gray and orange shadings indicate the large and small triangles formed by Nb atoms, with X atoms at the center of these triangles labeled as X-l and X-s, shown by pink and purple balls, and the remaining X atoms are represented by light brown balls. The brown arrow and "P" denote the polarization direction. The red and blue arrows represent the nearest-neighbor and next-nearest-neighbor exchange couplings between Nb_3 trimers. The gray dash lines indicate the Nb–Nb distance within (d_{Nb1}) and between (d_{Nb2}) trimers. d_{XS} and d_{XL} represent the vertical displacements of corresponding X relative to Nb atomic layer, while Δ_S and Δ_L represent the vertical displacements of X-s and X-l atoms relative to the other three halogens in the same sublayer. (d) Electronic configuration of $[Nb_3]^{8+}$. [(e) and (f)] Band structures of Nb_3Cl_8 in NM (e) and FM (f) configurations. In (f), the blue and red bands represent the spin-up and spin-down channels. (g) Band gaps at the Γ point as a function of Hubbard U, calculated using the magnetic ground states.

TABLE I. Lattice constants (a), Nb–Nb distance within (d_{Nb1}) and between (d_{Nb2}) Nb_3 trimers, vertical shift of X atoms [see Fig. 1(c)], polarization (P), magnetic ground states (G. S.), and the nearest-neighbor (J_1) and next-nearest-neighbor (J_2) exchange couplings between Nb_3 trimers (in units of meV/Nb_3) for monolayer Nb_3X_8. Here, the magnetic coupling between Nb atoms within a Nb_3 trimer is FM. A positive value of the exchange constant indicates AFM coupling.

Halides	a (Å)	$d_{Nb1/2}$ (Å)	$\Delta_{S/L}$ (Å)	$d_{XS/L}$ (Å)	Δ_S/d_{XS}	Δ_L/d_{XL}	P (pC/m)	G. S	J_1/J_2 (meV/Nb_3)
Nb_3F_8	5.95	2.59/3.36	0.48/0.23	1.10/1.35	0.44	0.17	1.26	ZZ	6.75/−0.49
Nb_3Cl_8	6.76	2.81/3.95	0.47/0.29	1.36/1.64	0.35	0.18	0.21	FM	0.12/−0.24
Nb_3Br_8	7.11	2.88/4.23	0.54/0.35	1.44/1.76	0.38	0.20	0.41	FM	−2.74/−0.37
Nb_3I_8	7.63	3.01/4.62	0.60/0.47	1.54/1.91	0.39	0.25	0.56	FM	−2.93/−0.82

suggested by hybrid functionals (HSE06),[31,54] *meta*-GGA (SCAN),[55] and DMFT.[29,31,56]

B. Stacking dependent geometry and stability of Nb_3X_8 bilayers

We next investigate how interlayer couplings reshape the geometric and electronic structures of bilayer Nb_3X_8. As the monolayer exhibits an intrinsic OOP polarization, the two layers can stack in three alignments, namely, up–up [Fig. S11(f)], up–down [Fig. 2(a)], and down–up [Figs. S5(b) and S5(c)], which are labeled as UU, UD, and DU, respectively. Lateral stacking registries further differentiate the stackings. Figures 2(b) and 2(c) present the top-views of the up- and down-polarized bottom Nb_3X_8 layers, respectively, in which interfacial X and Nb atoms are highlighted and the outer X atoms are faded for clarity. We identify four inequivalent interfacial X triangles (shadowed in orange) with their hollow sites labeled 1 to 4, in either up- or down-polarization case. Taking the X-s atom of the

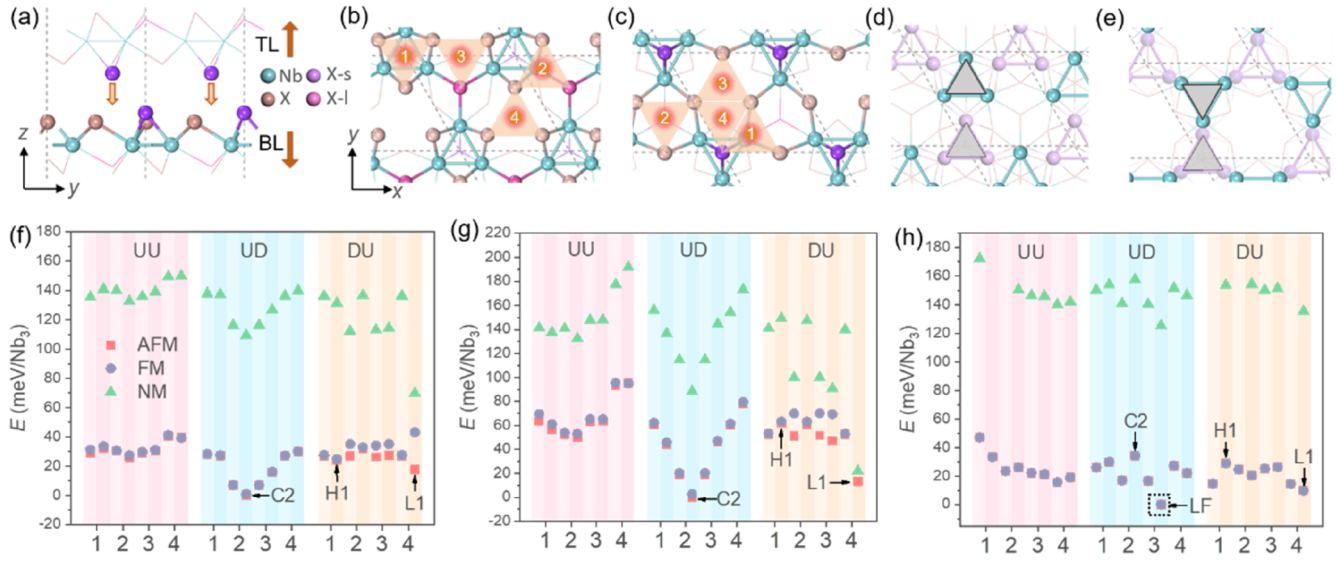

FIG. 2. (a) Side view of the fully relaxed atomic structure of a Nb_3X_8 bilayer. Interfacial X-s atoms of the top layer and all interfacial X and Nb atoms of the bottom layer are highlighted, while other atoms are represented using lines. The brown arrows indicate the polarization directions of the top (TL) and bottom (BL) layers, respectively. [(b) and (c)] Top-views of the atomic structure of the bottom layer in up- and down-polarizations, respectively. The shadowed numbers 1–4 mark four inequivalent X-hollow positions at the interface. All X atoms in the surface sublayer are blurred using line models. [(d) and (e)] Schematics of untwisted (R0, d) and 60° twisted (R60, e) bilayers. All X atoms are blurred using lines to highlight the relative position of top (light sea green) and bottom (light purple) layer Nb atoms. The gray shadowed triangles indicate Nb_3 trimers. [(f)–(h)] Energies of all 24 stacking configurations for bilayer Nb_3Cl_8 (f), Nb_3I_8 (g), and Nb_3F_8 (h) with a 1.2 eV U value (h). The square, circle, and triangle symbols represent interlayer AFM, FM, and NM, respectively. The notation ZZ represents the intralayer zigzag magnetic configuration. The red, blue, and yellow shadowed blocks represent polarization directions of UU, UD, and DU, respectively. The light and dark shaded blocks represent R0 and R60, respectively. The energy of the most stable stacking in each material is set as the reference (zero) energy.

top layer as a reference for alignment UD (for alignments UU and DU, we take the X-l atom), sliding the top layer to align the X-s (or X-l) atom occupying any one of these sites constructs four distinct stacking configurations. A third degree of freedom is the relative twist between the two layers. We considered untwisted (R0) and 60° twisted [R60 bilayers, as shown in Figs. 2(d) and 2(e)], respectively. Combining polarization (three alignments) with hollow site (four sites) and twist angle (two angles) yields 24 distinct stacking configurations per halide. We label them as (site)-(twist)-(polarization); for instance, 1-R0-UU corresponds to the AA stacking. Within this scheme, configurations 1-R60-DU, 4-R60-DU, and 2-R60-UD correspond to the experimentally observed H1 and L1 stackings in the high- (HT) and low-temperature (LT) phases, and their common stacking C2 of bulk Nb_3X_8, respectively (Fig. S4).[33,34,57–59]

Figures 2(f)–2(h) and S6 depict the total energies of all 24 Nb_3X_8 bilayer stackings in the NM, interlayer FM, and interlayer AFM configurations, while Fig. S8 presents the corresponding interlayer distances. The four halides exhibit halogen-dependent trends in their relative energy profiles. For Nb_3Cl_8, Nb_3Br_8 and Nb_3I_8, the global energy minimum corresponds to the 2-R60-UD stacking (C2), whereas Nb_3F_8 favors the 3-R60-UD (LF) configuration over C2. The preference of C2 in Nb_3Cl_8 to Nb_3I_8 rationalizes the experimentally observed bilayer dimerization (with the C2 stacking) in their LT and HT bulk forms. By contrast, Nb_3F_8 is expected to adopt a different pairing registry. Because the C2 (or LF) stacking adopts a UD polarization alignment, the stacking registry between paired C2 bilayers in bulk Nb_3X_8 must be of the DU alignment. Among all DU configurations [colored yellow in Figs. 2(f)–2(h) and S5], the L1 stacking is consistently the most stable, while H1 is the second-lowest in energy only for Nb_3Cl_8. For Nb_3Cl_8, Nb_3Br_8, and Nb_3I_8, our bilayer total-energy calculations identify L1 and C2 as the lowest-energy configurations among the considered DU and UD stackings, respectively. This energetic preference is consistent with experimental observations that the LT phases adopt alternating L1 and C2 stackings.[33,34,59,60] Notably, the identity of the most stable stackings does not change upon inclusion of U = 1.2 eV (Fig. S6). For other DU stackings related to L1 (1-R60-DU) by in-plane sliding, the most stable registry is 2-R60-DU for Nb_3F_8 and 3-R60-DU for Nb_3Br_8 and Nb_3I_8. These results suggest that bulk Nb_3F_8 in its LT phase adopts an interleaved sequence of LF (3-R60-UD) and L1 bilayers, a geometry distinct from the C2-based stacking sequences found in the heavier halides. However, we note that several other stackings lie very close in energy (for example, among the UD configurations of Nb_3Cl_8, five stackings are at most 3.5 meV/Nb_3 higher in energy than the H1 state), so at finite temperatures, the favored stacking configuration is governed by the free energy, $F = E - TS$. Thus, entropic contributions TS might render higher-energy stackings thermodynamically accessible. Indeed, the H1 stacking, slightly less stable than L1 in Nb_3Cl_8 and Nb_3Br_8, was reported to constitute the high-temperature phase alongside the C2 stacking. This provides a likely route to stacking disorder in real samples.

In Nb_3F_8 bilayers, the LF (3-R60-UD) stacking is most stable, rather than the most favored C2 (2-R60-UD) configuration in Nb_3Cl_8, Nb_3Br_8, and Nb_3I_8, highlighting the distinct structural preference of Nb_3F_8. In each UD configuration, the interfacial halogen atoms of the bottom layer define four inequivalent triangles [highlighted by orange shadows in Fig. 2(c)], with their side lengths listed in Table S3. For Nb_3Cl_8, Nb_3Br_8, and Nb_3I_8, all four triangles have comparable sizes and Triangle 2 has relatively the longest side, corresponding to the lowest electronic density within the triangle. When the top-layer X-s atom is positioned above this triangle site, the Coulomb repulsion between interfacial halogens is minimized, yielding the lowest interfacial energy and the shortest interlayer distance in the 2-R60-UD stacking (Fig. S8). In contrast, these four triangles undergo such substantial disproportionation in Nb_3F_8 that Triangle 2 becomes the most compressed (2.82 Å), while Triangle 3 expands to the largest size (3.12 Å). Following the same size-density relation, the reduced electron density of Triangle 3 stabilizes the stacking in which the upper X-s atom is located above it, i.e., the 3-R60-UD (LF) configuration. This explains why Nb_3F_8 favors the LF stacking, in contrast to the C2 preference of the heavier halides.

C. Role of interlayer coupling in electronic structures and Mottness

We next take bilayer Nb_3Cl_8 in the representative L1 (4-R60-DU) stacking configuration as a prototype to elucidate the role of interlayer coupling in modulating electronic structures. Previous studies suggested that the L1 stacking configuration hosts a NM ground state;[31,61] we, therefore, begin with the NM case. Figure 3(a) plots an NM bandstructure of bilayer Nb_3Cl_8. Compared with the isolated monolayer, where partially filled flat bands appear near the Fermi level, stacking two layers splits these bands into a fully occupied valence band (VB1) and an empty conduction band (CB1). Both remain spin-degenerate and lie close to the Fermi level. Wavefunction norm visualizations indicate that VB1 corresponds to a bonding state between the two interfacial Cl sublayers [Fig. 3(b)], while CB1 is the corresponding antibonding state [Fig. 3(c)]. This interlayer orbital hybridization gives rise to the observed splitting of the flat bands in the NM bilayer.

Compared with the NM band structure shown in Fig. 3(a), the corresponding spin polarized bandstructure with the interlayer AFM coupling is shown in Fig. 3(d). This AFM state is lower in energy by 19.4 meV/Nb_3. As in the NM case, there are two flat bands residing near the Fermi level, one is a fully occupied valence band (VB1) and the other is an empty conduction band (CB1), separated by a 0.40 eV gap at Γ. Each band is spin-degenerate in energy but spatially separated for different spins. Visualized wavefunction norms at Γ [Figs. 3(e) and 3(f)] and layer-projected DOS [Fig. 3(g)] clearly demonstrate this layer-dependent spin locking: the spin-up component of VB1 predominantly localizes on the bottom layer [Fig. 3(e)], while the spin-down component resides mainly on the top layer [Fig. 3(f)]. A similar layer–spin separation holds for CB1, where the spatial distributions of spin-up and spin-down states mirror those in VB1 [Figs. S8(a) and S8(b)]. Consequently, each layer hosts

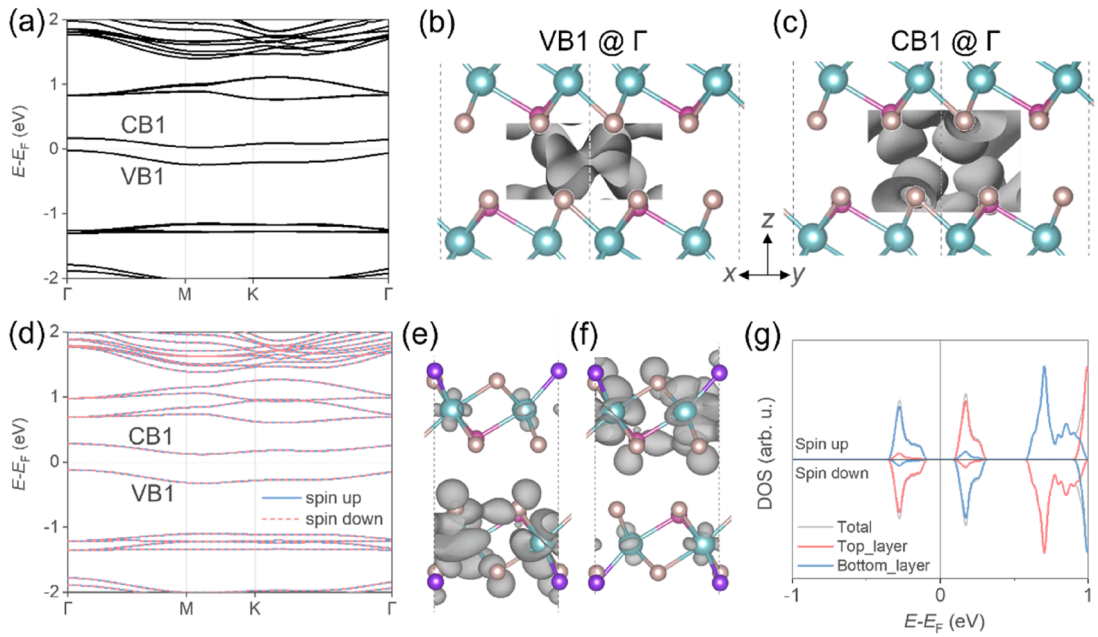

FIG. 3. (a) Electronic band structure of Nb_3Cl_8 with L1 stacking in the NM state. [(b) and (c)] Side views of Nb_3Cl_8 with L1 stacking. (d) Electronic band structure of Nb_3Cl_8 with L1 stacking in the interlayer AFM state. The isosurface represents the visualized wavefunction norms of the VB1 (b) and CB1 (c) at the Γ point. The isosurface value was set to 3×10^{-4} e/bohr^3. [(e) and (f)] Visualized wavefunction norms of the VB1 for spin-up (g) and spin-down (h) components. The isosurface value was set to 5×10^{-4} e/bohr^3. (g) Layer-projected density of states (DOS) for the AFM configuration of L1 stacking, where red and blue lines represent projections onto the top and bottom layers.

energetically separated spin-polarized states that align oppositely across the bilayer, consistent with the characteristic of an AFM-coupled Mott insulator. Furthermore, the bandgaps at Γ and the global band gaps increase linearly with the applied Hubbard U value [Figs. S9(g) and S9(h)], identifying it as a Mott–Hubbard gap, with VB1 and CB1 corresponding to the lower- (LHB) and upper-Hubbard bands (UHB), respectively. This linear U-dependence is universal across all 24 stacking configurations of each halide bilayers, as demonstrated by representative C2, L1, and H1 stacking orders of bilayer Nb_3Cl_8 in Figs. S7(g) and S7(h). These results show the robustness of the Mott insulator state in Nb_3X_8 bilayers, which is consistent with the Mott gaps observed via ARPES measurements.

This robust Mottness arises from the dominance of on-site Coulomb interactions over interlayer hopping. In Nb_3X_8, the half-filled states are highly localized on the Nb d-orbitals and the interlayer coupling is mediated primarily via the interfacial halogen (X) atoms. Thus, the interlayer hybridization is relatively weak compared with the Coulomb repulsion. As a quantitative example, the bonding–antibonding splitting at Γ in the nonmagnetic L1-stacked Nb_3Cl_8 bilayer is 0.19 eV [Fig. 3(a)], while the Coulomb-driven gap is ~0.40 eV [Fig. 3(d)]. Because the Coulomb energy scale substantially exceeds the interlayer hopping scale, correlation effects dominate and the bilayer remains correlation driven rather than becoming a simple band insulator.

We next examine Nb_3Cl_8 in the representative C2 and L1 stackings to illustrate how different polarization alignments affect the electronic structures. Stacking C2 corresponds to the experimentally observed bilayer dimers. Figures 4(a) and 4(b) depict its structure and interlayer differential charge density (DCD) in the side- and top-views. In this configuration, the interfacial X-s atoms (violet balls) undergo charge depletion (aqua contours), while the three nearest halogen atoms in the opposite layer [assigned to Triangle

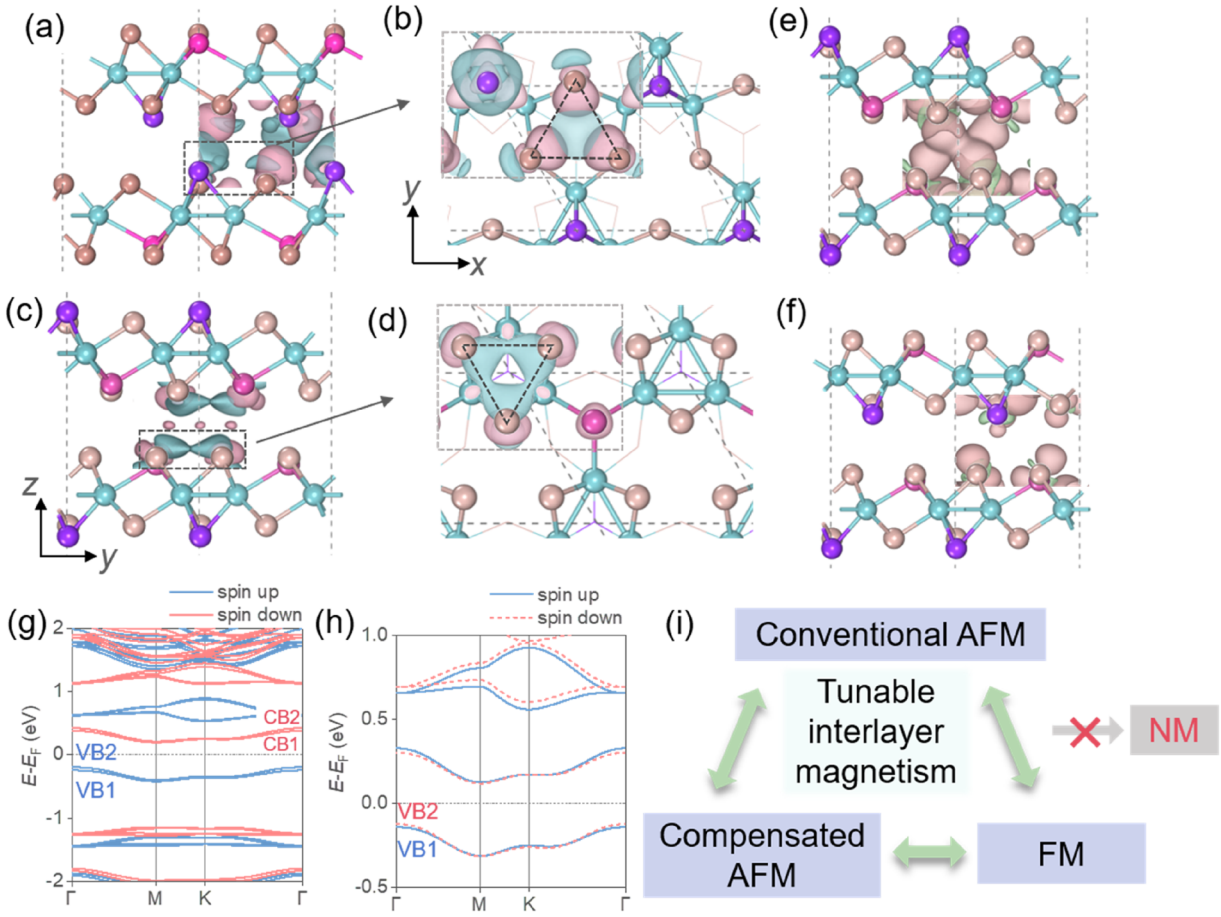

FIG. 4. (a) Side view of the C2 stacking of Nb_3Cl_8. The isosurface represents the interfacial differential charge density (DCD), with red indicating charge accumulation and aqua indicating charge reduction. (b) Top view of the DCD from the dashed box in (a). [(c) and (d)] Same as (a) and (b) but for the L1 stacking of Nb_3Cl_8. [(e) and (f)] Side view of the L1 (e) and 4-R60-UU (f) stacking of Nb_3Cl_8. The isosurface represents the spin density in the interlayer FM coupling configuration, with orange for spin-up and green for spin-down. (g) Band structure of Nb_3Cl_8 with 4-R60-UU stacking in the FM configuration. (h) Band structure of Nb_3Cl_8 with AA (1-R0-UU) stacking in the AFM configuration. (i) Illustration of tunable interlayer magnetism in the Nb_3X_8 system. The interlayer DCDs are shown with an isosurface value of 1×10^{-4} e/bohr^3. The spin densities are shown with an isosurface value of 5×10^{-4} e/bohr^3.

2 in Fig. 2(c), highlighted by black dashed triangle in Fig. 4(b)] accumulate charge (red contours). This charge redistribution establishes local electric dipoles oriented along the vertical direction. These oppositely aligned dipoles enhance the electrostatic attraction across the interface, thereby substantially strengthening the interlayer binding. We then turn to the L1 stacking, which represents the relative arrangement between neighboring C2 dimers in the LT phase of Nb_3Cl_8. Figures 4(c) and 4(d) depict its structure and DCD. At the interface, the two Triangle 2 units [Fig. 2(b), highlighted by a black dashed triangle in Fig. 4(d)] from the top and bottom layers, respectively, are aligned with a relative angle of 60°. Within these triangles, the electronic density is depleted (aqua contours), while excess charge densities (red contours) redistribute primarily to the surrounding regions and partially into the interlayer space. The reduced charge density inside the triangles weakens Coulomb repulsion among the three halogen atoms, leading to a contraction of the triangle side length from 3.42 Å in the monolayer to 3.34 Å in the bilayer. At the same time, charge accumulation in the interlayer region further enhances the electrostatic attraction between the two layers, making the L1 stacking energetically most favorable in DU configurations.

D. Tunable interlayer magnetism

We further examine how interlayer coupling modulates the preferred magnetic order in Nb_3X_8 bilayers. Total energy comparisons among different magnetic states [Figs. 2(f)–2(h) and S6] reveal that most (71 out of 96) stackings strongly favor interlayer AFM, while 22 out of 96 exhibit nearly degenerate interlayer AFM and FM energies with energy differences below 0.1 meV/Nb_3. These results remain relatively robust across a U range of 0.6–1.8 eV, as demonstrated by the tests in Fig. S7. Notably, interlayer FM is stabilized in the 4-R60-UU stacking of Nb_3Cl_8, Nb_3Br_8, and Nb_3I_8 [Fig. 4(f)]. To clarify the mechanism, we use the L1 and 4-R60-UU stackings of Nb_3Cl_8 as prototypical examples. In the L1 stacking, the energy difference E_{FM}-E_{AFM} is 23.4 meV/Nb, the largest among all stackings. The FM spin density [Fig. 4(e)] exhibits significant interlayer overlap, which enhances Pauli repulsion. This repulsion favors interlayer AFM and outweighs the FM tendency from interlayer hopping, stabilizing a robust interlayer AFM ground state.[62] In the 4-R60-UU stacking, by contrast, the interlayer overlap is largely suppressed [Fig. 4(f)], substantially weakening the Pauli repulsion. Thus, the dominant interlayer hopping leads to the interlayer FM coupling.[62] The FM band structure plotted in Fig. 4(g) shows a 49 meV splitting of the two VBs (noted VB1 and VB2) at the Γ point (42 meV for the two CBs, noted CB1 and CB2), while VB1 and VB2 remain degenerate at the K point. The visualized wavefunction norm at K confirms that the spin-up component of VB1 coincides with the spin-down component of CB1 [Figs. S11(b)–S11(e)], consistent with the characteristics of a Mott insulating state. Thus, interlayer magnetism is governed by stacking-dependent variations in interfacial orbital overlap, which, in turn, modulate the relative strength of Pauli repulsion and interlayer hopping. Their competition leads to robust AFM states, robust FM states, or nearly degenerate AFM–FM configurations.

Among the 71 AFM-favored configurations, at least two distinct types emerge. In all R60-twisted stackings with antiparallel polarization alignments (up to eight stacking per halide), an inversion symmetry connects the two spin sublattices, resulting in conventional AFM states with spin-degenerate bands developing throughout the Brillouin zone (BZ) [see Fig. S5(c) for the L1 stacked Nb_3Cl_8 bilayer]. However, every UU-polarized or untwisted (R0) stacking (up to 16 stackings per halide) lacks such symmetry, leading to compensated AFM[63] states. These states exhibit finite spin splitting between the spin-up and spin-down bands across the entire Brillouin zone. The simplest case is the AA stacking (1-R0-UU). Its band structure [Fig. 4(h)] shows a splitting of up to 26 meV among the four bands near the Fermi level, particularly in VB1 and VB2 at Γ. Therefore, Nb_3X_8 bilayers realize a wide range of stacking-tunable interlayer magnetism, spanning FM, near-degenerate AFM/FM, conventional AFM, and compensated AFM [Fig. 4(i)]. Although direct electric-field switching of polarization in Nb_3Cl_8 remains challenging, combining electric fields with thermal activation, tensile strain, charge doping, or scanning-probe-tip manipulation offers promising routes to control interlayer magnetism.

Our calculations reveal that both the C2 and H1 stackings, which constitute the HT bulk phases of Nb_3Cl_8 and Nb_3Br_8, exhibit interlayer AFM coupling, aligning with the AFM behavior experimentally observed in these HT phases. However, experiments report an NM ground state for the LT phases.[31,33,34] Two microscopic mechanisms were proposed to explain the origin of this NM behavior, namely inter-layer charge disproportionation[33] and the formation of a band insulator through interlayer interactions.[34,51] Although DFT is not designed to fully capture PM states, it can directly describe non-magnetic states arising from either of these mechanisms. Because both mechanisms rely on interlayer coupling, the minimal structural unit that can host them is a bilayer. However, our exhaustive DFT calculations for all bilayer stackings of the four Nb_3X_8 halides revealed neither charge disproportionation nor band insulating behavior.

We further optimized the LT-phase geometric structures of bulk Nb_3Cl_8 and Nb_3Br_8 using the NM configuration and then compared their energies in NM, interlayer AFM, and FM states (Table S4). In every case, the interlayer AFM state is energetically more favored than the NM and interlayer FM states. The energy difference E_{NM}-E_{AFM} increases monotonically with the on-site Hubbard U, consistent with our bilayer results (Table S4). Moreover, the HSE06-calculated bandgap for the AFM high-temperature phase [1.1 eV, Fig. S12(b)] aligns well with the experimentally reported optical gap of ~1.2 eV.[31] These findings indicate that, within the DFT(+U) framework, the LT ground state of bulk Nb_3Cl_8 and Nb_3Br_8 is most plausibly an interlayer AFM Mott insulator. This interpretation is not inconsistent with the nearly featureless LT susceptibility observed experimentally. However, if the true ground state is strictly NM, we attribute this discrepancy to strong quantum spin fluctuations and geometric spin frustration that suppress long-range order in experiments. Such dynamical effects are not fully captured by static DFT, which calls for a more complete many-body description.

III. CONCLUSION

In summary, we found that all considered Nb_3X_8 bilayers are robust Mott insulators, with the bandgap increasing linearly with the Hubbard U. The interlayer magnetic ground state is governed by the competition between Pauli repulsion and interlayer hopping:

most stacking configurations stabilize interlayer AFM order, while a smaller fraction favor FM or show nearly degenerate AFM-FM states. Symmetry analysis reveals two distinct classes of interlayer AFM: conventional AFM and compensated AFM, the latter maintaining zero net magnetization yet exhibiting pronounced spin splitting in the band structure. Across all stackings, the nonmagnetic state is energetically unfavorable. Extending these insights to bulk Nb_3Cl_8 and Nb_3Br_8, we predict interlayer AFM Mott insulating ground states in their low-temperature phases within the DFT(+U) framework. Altogether, these findings highlight breathing kagome bilayers as a versatile platform where robust Mottness intertwines with stacking-dependent interlayer magnetism, thereby offering new opportunities for tuning correlated phases through interlayer engineering.

IV. METHODS

Our density functional theory (DFT) calculations were performed using the generalized gradient approximation (GGA) for the exchange-correlation potential in the form of Perdew–Burke–Ernzerhof (PBE),[64] the projector augmented wave method,[65] and a plane wave basis set as implemented in the Vienna *ab initio* simulation package (VASP).[66] The dispersion correction was included using Grimme's semiempirical D3 scheme (with zero damping)[67] in combination with the PBE functional (PBE-D3). A kinetic energy cutoff of 450 eV for the plane wave basis sets was adopted for all structural relaxations and electronic structure calculations. All atoms were allowed to relax until the residual force per atom is below 0.01 eV/Å. A vacuum layer exceeding 15 Å in thickness was used to reduce imaging interactions from neighboring supercells. Gamma-centered Monkhorst–Pack k-meshes of 5 × 5 × 1 and 9 × 9 × 1 were used to sample the Brillouin zone of 1 × 1 unit cells for structural relaxations and electronic structure calculations, respectively. For energy comparisons among magnetic configurations, a 2 × $\sqrt{3}$ supercell and a 4 × 5 k-mesh were employed. A Gaussian smearing width of 0.01 eV was used to smooth the distribution function of electronic states in all calculations. A DFT+U method implemented using the rotationally invariant approach[68] with U = 1.2 eV was employed for Nb 3d orbitals, following the previous study.[31] Although linear response yielded higher values (1.64–1.84 eV for monolayer Nb_3X_8),[69] we adopted 1.2 eV to account for the typical overestimation of U by the linear response method. The comparison of energies of different magnetic configurations was made based on the structures optimized for interlayer AFM coupling. Energy comparison based on the structures relaxed using interlayer FM does not change the relative energetic stability. The convergence of the magnetic configurations and magnetic anisotropy energy with respect to computational details has been tested, as shown in Fig. S2.

Spin-exchange coupling parameters were extracted based on a Heisenberg model as follows:

$$H = H_0 + J_1 \sum_{\langle i \neq j \rangle} \vec{S_i} \cdot \vec{S_j} + J_2 \sum_{\langle\langle i \neq j \rangle\rangle} \vec{S_i} \cdot \vec{S_j}.$$

Here, J_1 and J_2 represent the nearest-neighbor and next-nearest-neighbor magnetic couplings, respectively, as illustrated in Figs. 1(b) and S1(d).

Note added in proof. While preparing this manuscript, we came across Ref. 61, which reports on the layer-dependent evolution of the electronic structure in multilayer Nb_3Cl_8.

SUPPLEMENTARY MATERIAL

For calculation details regarding the magnetic ground states and magnetic anisotropy of monolayer Nb_3X_8, as well as the atomic and electronic structures of the monolayers, multilayers, and bulk phases mentioned in the main text, please refer to the supplementary material.

ACKNOWLEDGMENTS

We gratefully acknowledge the financial support from the Ministry of Science and Technology (MOST) of China (Grant No. 2023YFA1406500) and the National Natural Science Foundation of China (Grant Nos. 92477205 and 52461160327). J.D. was supported by the Outstanding Innovative Talents Cultivation Funded Programs 2023 of Renmin University of China. Calculations were performed at the Physics Lab of High-Performance Computing (PLHPC) and the Public Computing Cloud (PCC) of Renmin University of China.

AUTHOR DECLARATIONS

Conflict of Interest

The authors have no conflicts to disclose.

Author Contributions

Zhongqin Zhang: Investigation (equal); Methodology (equal); Validation (equal); Visualization (equal); Writing – original draft (equal). **Jiaqi Dai**: Investigation (supporting); Project administration (supporting). **Cong Wang**: Supervision (equal); Writing – original draft (equal); Writing – review & editing (equal). **Zhihai Cheng**: Supervision (supporting). **Wei Ji**: Methodology (equal); Supervision (equal); Writing – original draft (equal); Writing – review & editing (equal).

DATA AVAILABILITY

The data that support the findings of this study are available within the article and its supplementary material. Additional data are available from the corresponding author upon reasonable request.

REFERENCES

[1] X. Han, H. Chen, H. Tan, Z. Cao, Z. Huang, Y. Ye, Z. Zhao, C. Shen, H. Yang, B. Yan, Z. Wang, and H.-J. Gao, Nat. Nanotechnol. **20**, 1017 (2025).
[2] J.-X. Yin, B. Lian, and M. Z. Hasan, Nature **612**, 647 (2022).
[3] Y. Wang, H. Wu, G. T. McCandless, J. Y. Chan, and M. N. Ali, Nat. Rev. Phys. **5**, 635 (2023).
[4] Z. Zhang, J. Dai, C. Wang, H. Zhu, F. Pang, Z. Cheng, and W. Ji, Adv. Funct. Mater. **35**, 2416508 (2025).
[5] S. Yan, D. A. Huse, and S. R. White, Science **332**, 1173 (2011).
[6] Z. Huang, H. Chen, Z. Zhang, H. Zhang, Z. Zhao, R. Wang, H. Yang, W. Ji, Z. Wang, and H.-J. Gao, "Spatially anisotropic Kondo resonance intertwined with superconducting gap in kagome metal $CsV_{3-x}Cr_xSb_5$," arXiv:2502.20735 (2025).

[7]H. Chen, H. Yang, B. Hu, Z. Zhao, J. Yuan, Y. Xing, G. Qian, Z. Huang, G. Li, Y. Ye, S. Ma, S. Ni, H. Zhang, Q. Yin, C. Gong, Z. Tu, H. Lei, H. Tan, S. Zhou, C. Shen, X. Dong, B. Yan, Z. Wang, and H.-J. Gao, Nature **599**, 222 (2021).
[8]C.-H. Liu, M. Wei, M. F. Cheung, and D. F. Perepichka, Chem. Mater. **34**, 3461 (2022).
[9]J. Dai, Z. Zhang, Z. Pan, C. Wang, C. Zhang, Z. Cheng, and W. Ji, "Kagome bands and magnetism in $MoTe_{2-x}$ kagome monolayers," Phys. Rev. B (published online 2026).
[10]W.-H. Ko, P. A. Lee, and X.-G. Wen, Phys. Rev. B **79**, 214502 (2009).
[11]T.-Y. Lin, F.-F. Song, and G.-M. Zhang, Phys. Rev. B **111**, 054508 (2025).
[12]H.-M. Jiang, M. Mao, Z.-Y. Miao, S.-L. Yu, and J.-X. Li, Phys. Rev. B **109**, 104512 (2024).
[13]T. Neupert, M. M. Denner, J.-X. Yin, R. Thomale, and M. Z. Hasan, Nat. Phys. **18**, 137 (2022).
[14]B. R. Ortiz, S. M. L. Teicher, Y. Hu, J. L. Zuo, P. M. Sarte, E. C. Schueller, A. M. M. Abeykoon, M. J. Krogstad, S. Rosenkranz, R. Osborn, R. Seshadri, L. Balents, J. He, and S. D. Wilson, Phys. Rev. Lett. **125**, 247002 (2020).
[15]Y. Xing, J. Shen, H. Chen, L. Huang, Y. Gao, Q. Zheng, Y.-Y. Zhang, G. Li, B. Hu, G. Qian, L. Cao, X. Zhang, P. Fan, R. Ma, Q. Wang, Q. Yin, H. Lei, W. Ji, S. Du, H. Yang, W. Wang, C. Shen, X. Lin, E. Liu, B. Shen, Z. Wang, and H.-J. Gao, Nat. Commun. **11**, 5613 (2020).
[16]N. Morali, R. Batabyal, P. K. Nag, E. Liu, Q. Xu, Y. Sun, B. Yan, C. Felser, N. Avraham, and H. Beidenkopf, Science **365**, 1286 (2019).
[17]D. F. Liu, A. J. Liang, E. K. Liu, Q. N. Xu, Y. W. Li, C. Chen, D. Pei, W. J. Shi, S. K. Mo, P. Dudin, T. Kim, C. Cacho, G. Li, Y. Sun, L. X. Yang, Z. K. Liu, S. S. P. Parkin, C. Felser, and Y. L. Chen, Science **365**, 1282 (2019).
[18]M. Jovanovic and L. M. Schoop, J. Am. Chem. Soc. **144**, 10978 (2022).
[19]I. Piquero-Zulaica, W. Hu, A. P. Seitsonen, F. Haag, J. Küchle, F. Allegretti, Y. Lyu, L. Chen, K. Wu, Z. M. A. El-Fattah, E. Aktürk, S. Klyatskaya, M. Ruben, M. Muntwiler, J. V. Barth, and Y. Zhang, Adv. Mater. **36**, 2405178 (2024).
[20]Z. Shi and N. Lin, J. Am. Chem. Soc. **131**, 5376 (2009).
[21]Y.-P. Mo, X.-H. Liu, and D. Wang, ACS Nano **11**, 11694 (2017).
[22]S. Furukawa, H. Uji-i, K. Tahara, T. Ichikawa, M. Sonoda, F. C. De Schryver, Y. Tobe, and S. De Feyter, J. Am. Chem. Soc. **128**, 3502 (2006).
[23]Z. Pan, W. Xiong, J. Dai, H. Zhang, Y. Wang, T. Jian, X. Cui, J. Deng, X. Lin, Z. Cheng, Y. Bai, C. Zhu, D. Huo, G. Li, M. Feng, J. He, W. Ji, S. Yuan, F. Wu, C. Zhang, and H.-J. Gao, Nat. Commun. **16**, 3084 (2025).
[24]L. Lei, J. Dai, H. Dong, Y. Geng, F. Cao, C. Wang, R. Xu, F. Pang, Z.-X. Liu, F. Li, Z. Cheng, G. Wang, and W. Ji, Nat. Commun. **14**, 6320 (2023).
[25]Q. Wu, W. Quan, S. Pan, J. Hu, Z. Zhang, J. Wang, F. Zheng, and Y. Zhang, Nano Lett. **24**, 7672 (2024).
[26]Z.-M. Zhang, B.-C. Gong, J.-H. Nie, F. Meng, Q. Zhang, L. Gu, K. Liu, Z.-Y. Lu, Y.-S. Fu, and W. Zhang, Nano Lett. **23**, 954 (2023).
[27]R. Wang, C. Wang, R. Li, D. Guo, J. Dai, C. Zong, W. Zhang, and W. Ji, Chin. Phys. B **34**, 046801 (2025).
[28]Y. Zhang, Y. Gu, H. Weng, K. Jiang, and J. Hu, Phys. Rev. B **107**, 035126 (2023).
[29]M. Date, F. Petocchi, Y. Yen, J. A. Krieger, B. Pal, V. Hasse, E. C. McFarlane, C. Körner, J. Yoon, M. D. Watson, V. N. Strocov, Y. Xu, I. Kostanovski, M. N. Ali, S. Ju, N. C. Plumb, M. A. Sentef, G. Woltersdorf, M. Schüler, P. Werner, C. Felser, S. S. P. Parkin, and N. B. M. Schröter, Nat. Commun. **16**, 4037 (2025).
[30]J. Hu, X. Zhang, C. Hu, J. Sun, X. Wang, H.-Q. Lin, and G. Li, Commun. Phys. **6**, 172 (2023).
[31]S. Gao, S. Zhang, C. Wang, S. Yan, X. Han, X. Ji, W. Tao, J. Liu, T. Wang, S. Yuan, G. Qu, Z. Chen, Y. Zhang, J. Huang, M. Pan, S. Peng, Y. Hu, H. Li, Y. Huang, H. Zhou, S. Meng, L. Yang, Z. Wang, Y. Yao, Z. Chen, M. Shi, H. Ding, H. Yang, K. Jiang *et al.*, Phys. Rev. X **13**, 041049 (2023).
[32]S. Grytsiuk, M. I. Katsnelson, E. G. C. P. van Loon, and M. Rösner, npj Quantum Mater. **9**, 8 (2024).
[33]Y. Haraguchi, C. Michioka, M. Ishikawa, Y. Nakano, H. Yamochi, H. Ueda, and K. Yoshimura, Inorg. Chem. **56**, 3483 (2017).
[34]J. P. Sheckelton, K. W. Plumb, B. A. Trump, C. L. Broholm, and T. M. McQueen, Inorg. Chem. Front. **4**, 481 (2017).
[35]Y. Z. Zhou, X. Han, J. Luo, D. T. Wu, A. F. Fang, B. Shen, B. J. Feng, Y. G. Shi, J. Yang, and R. Zhou, Chin. Phys. Lett. **42**, 037303 (2025).
[36]Z. Sun, H. Zhou, C. Wang, S. Kumar, D. Geng, S. Yue, X. Han, Y. Haraguchi, K. Shimada, P. Cheng, L. Chen, Y. Shi, K. Wu, S. Meng, and B. Feng, Nano Lett. **22**, 4596 (2022).
[37]Y. Zhao, J. Qiao, P. Yu, Z. Hu, Z. Lin, S. P. Lau, Z. Liu, W. Ji, and Y. Chai, Adv. Mater. **28**, 2399 (2016).
[38]J. Qiao, X. Kong, Z.-X. Hu, F. Yang, and W. Ji, Nat. Commun. **5**, 4475 (2014).
[39]A. Splendiani, L. Sun, Y. Zhang, T. Li, J. Kim, C.-Y. Chim, G. Galli, and F. Wang, Nano Lett. **10**, 1271 (2010).
[40]C. Wang, X. Zhou, L. Zhou, N.-H. Tong, Z.-Y. Lu, and W. Ji, Sci. Bull. **64**, 293 (2019).
[41]Z.-X. Hu, X. Kong, J. Qiao, B. Normand, and W. Ji, Nanoscale **8**, 2740 (2016).
[42]Z. Zhang, C. Wang, P.-J. Guo, L. Zhou, Y. Pan, Z. Hu, and W. Ji, Phys. Rev. B **111**, 054422 (2025).
[43]C. Wang, X. Zhou, Y. Pan, J. Qiao, X. Kong, C.-C. Kaun, and W. Ji, Phys. Rev. B **97**, 245409 (2018).
[44]P. Jiang, C. Wang, D. Chen, Z. Zhong, Z. Yuan, Z.-Y. Lu, and W. Ji, Phys. Rev. B **99**, 144401 (2019).
[45]B. Huang, G. Clark, E. Navarro-Moratalla, D. R. Klein, R. Cheng, K. L. Seyler, D. Zhong, E. Schmidgall, M. A. McGuire, D. H. Cobden, W. Yao, D. Xiao, P. Jarillo-Herrero, and X. Xu, Nature **546**, 270 (2017).
[46]L. Rogée, L. Wang, Y. Zhang, S. Cai, P. Wang, M. Chhowalla, W. Ji, and S. P. Lau, Science **376**, 973 (2022).
[47]L. Li and M. Wu, ACS Nano **11**, 6382 (2017).
[48]M. J. DelloStritto, A. D. Kaplan, J. P. Perdew, and M. L. Klein, APL Mater. **11**, 060702 (2023).
[49]L. A. Agapito, S. Curtarolo, and M. Buongiorno Nardelli, Phys. Rev. X **5**, 011006 (2015).
[50]M. S. Hybertsen and S. G. Louie, Phys. Rev. Lett. **55**, 1418 (1985).
[51]J. Dai, J. Qiao, C. Wang, L. Zhou, X. Wu, L. Liu, X. Song, F. Pang, Z. Cheng, X. Kong, Y. Wang, and W. Ji, Adv. Funct. Mater. **33**, 2302989 (2023).
[52]F. Conte, D. Ninno, and G. Cantele, Phys. Rev. Res. **2**, 033001 (2020).
[53]Y. Feng and Q. Yang, J. Mater. Chem. C **11**, 5762 (2023).
[54]J. Jiang, Q. Liang, R. Meng, Q. Yang, C. Tan, X. Sun, and X. Chen, Nanoscale **9**, 2992 (2017).
[55]J.-X. Xiong, X. Zhang, and A. Zunger, Phys. Rev. B **111**, 155122 (2025).
[56]J. Aretz, S. Grytsiuk, X. Liu, G. Feraco, C. Knekna, M. Waseem, Z. Dan, M. Bianchi, P. Hofmann, M. N. Ali, M. I. Katsnelson, A. Grubišić-Čabo, H. U. R. Strand, E. G. C. P. van Loon, and M. Rösner, Phys. Rev. X **15**, 041042 (2025).
[57]S. N. Magonov, P. Zoennchen, H. Rotter, H. J. Cantow, G. Thiele, J. Ren, and M. H. Whangbo, J. Am. Chem. Soc. **115**, 2495 (1993).
[58]B. J. Kim, B. J. Jeong, S. Oh, S. Chae, K. H. Choi, S. S. Nanda, T. Nasir, S. H. Lee, K.-W. Kim, H. K. Lim, L. Chi, I. J. Choi, M.-K. Hong, D. K. Yi, H. K. Yu, J.-H. Lee, and J.-Y. Choi, Phys. Status Solidi RRL **13**, 1800448 (2019).
[59]C. M. Pasco, I. El Baggari, E. Bianco, L. F. Kourkoutis, and T. M. McQueen, ACS Nano **13**, 9457 (2019).
[60]J. Kim, Y. Lee, Y. W. Choi, T. S. Jung, S. Son, J. Kim, H. J. Choi, J.-G. Park, and J. H. Kim, ACS Omega **8**, 14190 (2023).
[61]H. Liu, W. Li, Z. Zhou, H. Qu, J. Zhang, W. Hu, C. Wen, N. Wang, H. Deng, G. Li, and S. Yan, Phys. Rev. Lett. **135**, 076503 (2025).
[62]C. Wang, X. Zhou, L. Zhou, Y. Pan, Z.-Y. Lu, X. Wan, X. Wang, and W. Ji, Phys. Rev. B **102**, 020402(R) (2020).
[63]I. Mazin and PRX Editors, Phys. Rev. X **12**, 040002 (2022).
[64]J. P. Perdew, K. Burke, and M. Ernzerhof, Phys. Rev. Lett. **77**, 3865 (1996).
[65]P. E. Blöchl, Phys. Rev. B **50**, 17953 (1994).
[66]G. Kresse and J. Furthmüller, Phys. Rev. B **54**, 11169 (1996).
[67]S. Grimme, J. Antony, S. Ehrlich, and H. Krieg, J. Chem. Phys. **132**, 154104 (2010).
[68]S. L. Dudarev, G. A. Botton, S. Y. Savrasov, C. J. Humphreys, and A. P. Sutton, Phys. Rev. B **57**, 1505 (1998).
[69]M. Cococcioni and S. De Gironcoli, Phys. Rev. B **71**, 035105 (2005).